Letter

Integrated Flexible Microscale Mechanical Sensors Based on Cascaded Free Spectral Range-Free Cavities

Ye Luo,[#] Chunlei Sun,[#] Maoliang Wei, Hui Ma, Yingchun Wu, Zequn Chen, Hao Dai, Jialing Jian, Boshu Sun, Chuyu Zhong, Junying Li, Kathleen A. Richardson, Hongtao Lin, and Lan Li*

Read Online

ACCESS | ⬛ Metrics & More | 📖 Article Recommendations | 🔳 Supporting Information

ABSTRACT: Photonic mechanical sensors offer several advantages over their electronic counterparts, including immunity to electromagnetic interference, increased sensitivity, and measurement accuracy. Exploring flexible mechanical sensors on deformable substrates provides new opportunities for strain-optical coupling operations. Nevertheless, existing flexible photonics strategies often require cumbersome signal collection and analysis with bulky setups, limiting their portability and affordability. To address these challenges, we propose a waveguide-integrated flexible mechanical sensor based on cascaded photonic crystal microcavities with inherent deformation and biaxial tensile state analysis. Leveraging the advanced multiplexing capability of the sensor, for the first time, we successfully demonstrate 2D shape reconstruction and quasi-distributed strain sensing with 110 μm spatial resolution. Our microscale mechanical sensor also exhibits exceptional sensitivity with a detected force level as low as 13.6 μN in real-time measurements. This sensing platform has potential applications in various fields, including biomedical sensing, surgical catheters, aircraft and spacecraft engineering, and robotic photonic skin development.

KEYWORDS: *Integrated optics devices, Optical sensing and sensors, Optical resonators, Glass waveguides*
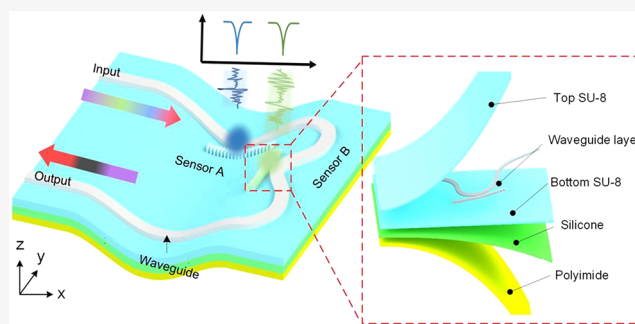

Photonic sensors are increasingly in demand in various fields, such as healthcare and medical monitoring,[1,2] industrial automation,[3] aerospace engineering,[4] and intelligent robotics,[5] due to their numerous advantages over their electronic counterparts[6−9] including compact footprints and superior sensitivity and accuracy, as well as the ability to perform multiplexing functions with immunity to electromagnetic interference (EMI). Photonic sensors typically measure and analyze how biological, chemical, and mechanical perturbations influence the optical parameters of the sensors. Among them, mechanical sensors have attracted great attention nowadays since they are widely employed to measure displacement, strain, force, acceleration, pressure, vibration, and ultrasound.[10−18] Optical microelectromechanical system (MEMS)-based sensors have made significant achievements,[15−17,19−21] but their rigid forms make them challenging to deploy flexibly for conformal sensing in three-dimensional space. To address this, fiber optic-based strategies have been developed for mechanical sensing due to their excellent intrinsic flexibility.[22−29] Nevertheless, realizing high-spatial-resolution detection of microstrain using discrete Bragg grating units is challenging due to their large device size.[30−33] Although distributed optical fiber sensors have the potential to achieve millimeter-level spatial resolution through time-domain,[34,35] frequency-domain,[36−38] and correlation-do-

main[39−41] scattering sensing mechanisms, they may exhibit limitations in sensitivity and accuracy compared to point sensing. Furthermore, implementing distributed fiber sensing technology can be complex and requires specialized and expensive equipment for spectral decoding and interpretation of measurement results, making them susceptible to disruptions caused by extraneous environmental noise.[5] Despite these trade-offs, mechanical sensing with high sensitivity and rapid, precise, and high-resolution measurements at the micrometer level hold substantial value for various applications. Numerous biological processes involve strain variations on the microscale, e.g., cell migration and differentiation,[42−44] wound healing,[45−47] and tumor progression.[48] In order to study biomechanics and develop intelligent composite materials and advanced medical devices,[49,50] real-time multi-point sensors with micron-level resolution can be integrated into high-value materials. One interesting example is the shape-sensing surgical catheter, which enables surgeons to easily
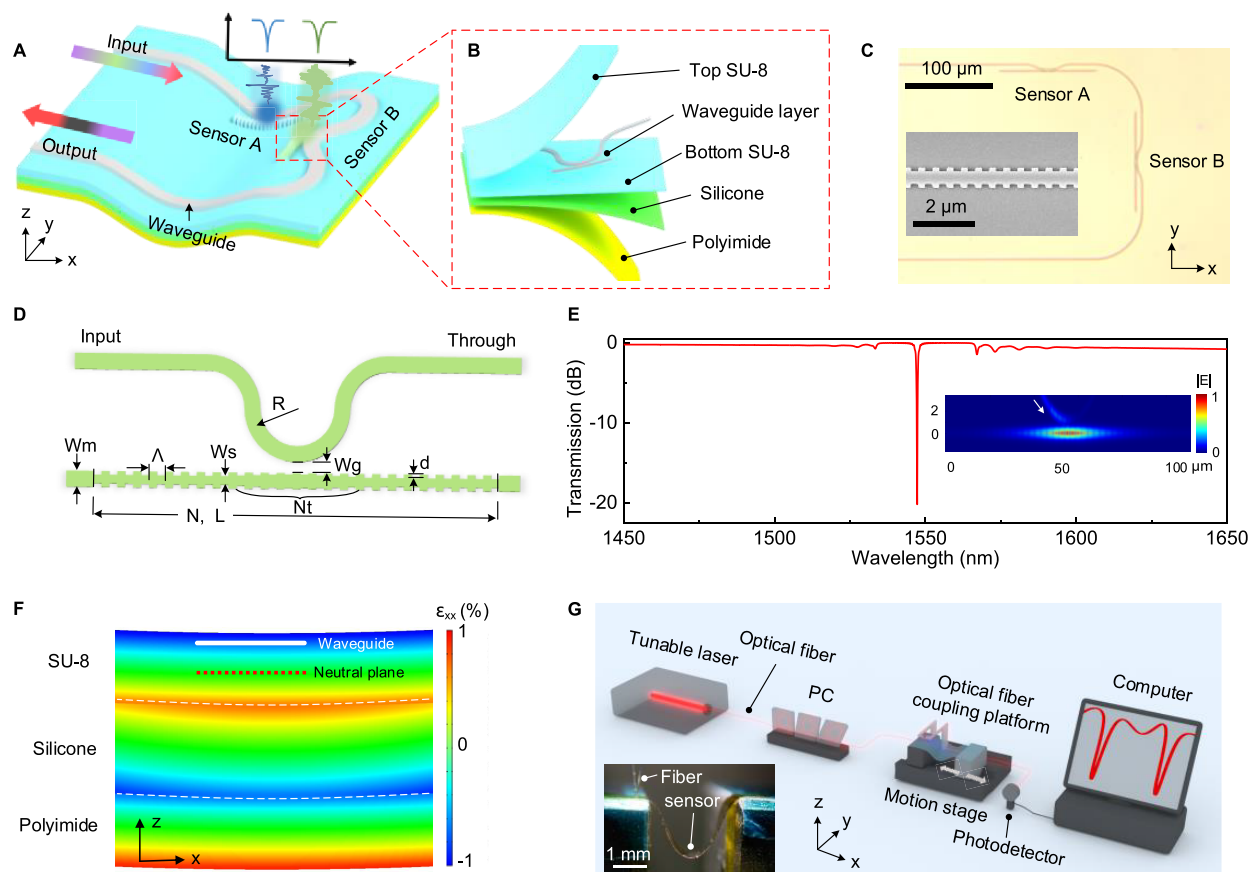
© 2023 American Chemical Society
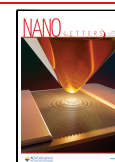
Figure 1. (A) Schematic of the flexible right-angle strain gauge with two strain sensors positioned perpendicular to each other. (B) Laminated structure of the flexible chip. The strain sensors are buried into the SU-8 cladding with double-layer silicone and polyimide tape as the mechanical support layer. (C) Microscopy image of the right-angle strain gauge. The inset shows the SEM image of the Bragg grating of the strain sensor. (D) Schematic of the strain sensor based on a side-coupled 1D PhC microcavity. (E) Simulated transmission spectrum of the side-coupled 1D PhC microcavity. The inset shows the electrical field component $|\mathbf{E}|$ for the fundamental quasi-TE mode at the resonant wavelength. (F) Contour plot of the principal strain along the x-axis in the xz plane of the flexible chip with a bending radius of 1 mm. The white dashed line denotes the boundaries of different layers. The white solid line indicates the position of the waveguide layer, while the red dashed line refers to the mechanical neutral plane. (G) Schematic diagram of the setup for device characterization. The inset shows the flexible chip mounted to a couple of linear motion stages with the strain sensor in the middle and the grating coupler placed on the static stage for fiber-to-chip coupling. PC: polarization controller.

navigate intricate anatomical pathways and perform minimally invasive surgeries in targeted areas.[51−54]

Recently, mechanically flexible photonic devices on deformable polymer substrates have emerged with potential applications in soft robotics, human motion monitoring, and human−machine interaction.[55−58] Over the past decade, significant research efforts have focused on free space-type flexible photonic sensors.[59−63] However, in most demonstrations, the requirements for free space light beam focusing/collimation equipment and spectrum analyzers have made flexible integration challenging for small-footprint, portable applications. Waveguide-integrated devices have the potential to exhibit much better performance characteristics than their free space counterparts, thanks to their tight optical confinement, convenient signal readout, and the ability to facilitate various functional components for integrated photonic circuits. In our previous works,[64,65] a suite of photonic devices, including flexible microdisk/microring resonators and photonic crystal (PhC) cavities, have been employed as strain sensors to investigate the strain−optical coupling behavior. These devices exhibit excellent optical performance, and extremely small changes in deformation and material parameters of the devices can produce a significant deviation

in optical properties such as a resonant wavelength shift. The sensitivity of such mechanical sensors can be deterministically regulated by changing the mechanical neutral plane (MNP) position within a multilayer polymer substrate and optimizing the design of optical sensing units.[66] Compared to the microdisk/microring resonators, one-dimensional (1D) PhC microcavities exhibit inherent deformation sensing advantages because of their mechanically variable unit lattices.[67,68] Such 1D architectures allow devices to detect various types and directions of strain with high precision.

In this paper, we propose a novel design for a microscale integrated flexible photonic mechanical sensor that boasts exceptional sensitivity and quasi-distributed sensing capabilities. The sensor incorporates cascaded 1D PhC microcavities embedded in a deformable polymer substrate. Here, the sensor units possess free spectral range (FSR)-free characteristics that enable quasi-distributed sensing through a single optical link via wavelength-division multiplexing (WDM) technology. Due to their low loss, compact footprint, and wide operating bandwidth characteristics, we demonstrate the integration of a large number of sensing units within a small, confined space.[69,70] As a conceptual demonstration, we integrated six sensor units with a shared single bus waveguide, allowing strain
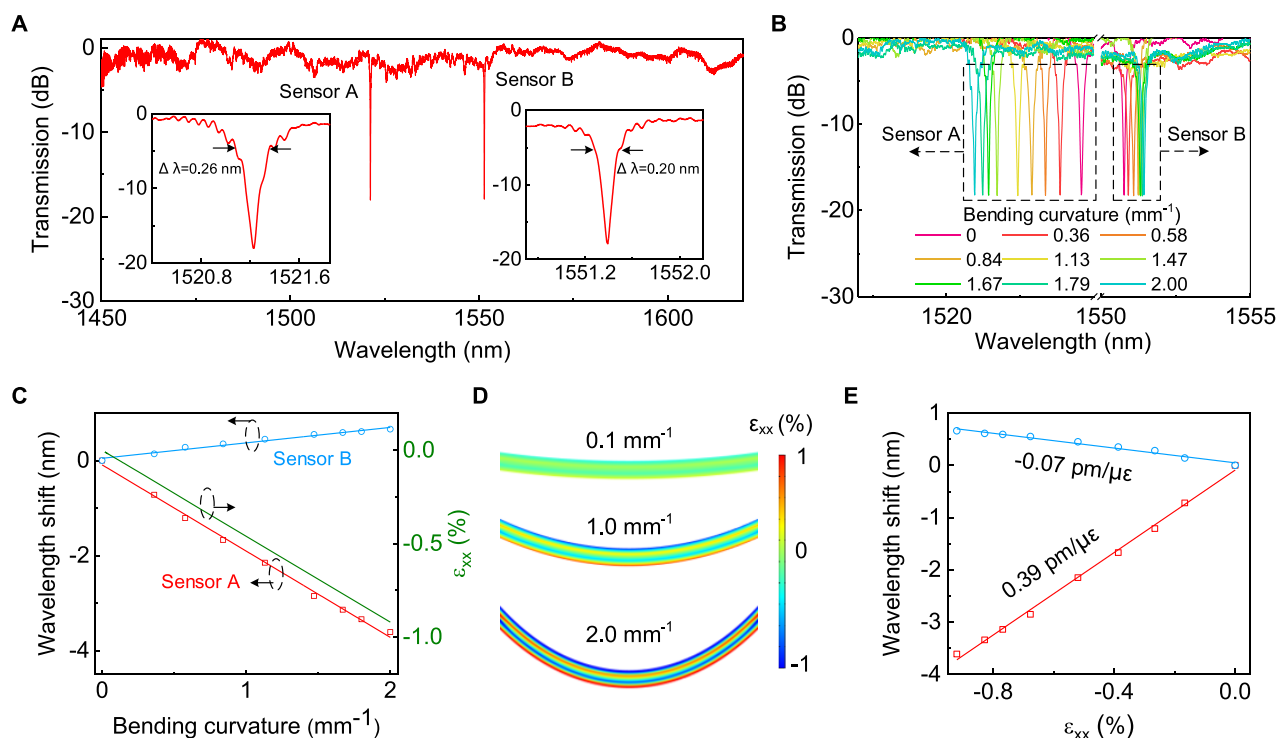
Figure 2. (A) Measured transmission spectra of the right-angle gauge without bending. Insets show the resonant dips of sensors A and B. (B) Measured transmission spectra of the right-angle gauge for different bending curvatures from 0 to 2 mm^{-1}. (C) Experimental resonant wavelength shift and simulated principal strain along the *x*-axis (ε_{xx}) for different bending curvature. (D) Simulated strain ε_{xx} for the bending curvature of 0.1, 1.0, and 2.0 mm^{-1}. (E) Relationship between the resonant wavelength shift of sensors A (red square) and B (blue circle) and strain ε_{xx}. The solid lines show the linear fitting results.

quasi-distribution detection in a buckling beam with a high spatial resolution of 110 μm. By utilizing the curvature information and optical feedback collected from the six sensing units at different locations, we successfully reconstructed the two-dimensional (2D) shape of a buckling beam. The demonstrated sensor exhibited high sensitivity with a detected force level as low as 13.6 μN in real-time measurements.

Typically, a single strain sensor can detect principal strain only in one direction. To broaden the capability for biaxial tensile analysis with predetermined principal directions, a right-angle strain gauge with two strain sensors positioned perpendicular to each other is used, as depicted in Figure 1A. Sensor A is positioned along the *x*-axis, while sensor B is positioned along the *y*-axis. Using a bus waveguide, both sensors with distinct resonant wavelengths can share it, allowing for a single optical test that determines the principal strain magnitudes with known directions. The laminated structure of the flexible chip is shown in Figure 1B, the waveguide layer is Ge$_{23}$Sb$_7$S$_{70}$ (GSS). The optical microscope image of the right-angle strain gauge is illustrated in Figure 1C; the inset shows a scanning electron microscopy (SEM) image of a Bragg grating. Our sensor unit utilizes a side-coupled 1D PhC microcavity with an FSR-free spectral response, as previously described in our work,[69] as shown in Figure 1D. The design and fabrication details are provided in Supporting Information Section S1. The sensor's transmission spectra were simulated using the three-dimensional finite difference time domain (3D FDTD) method with only one deep exhibited in the wavelength range from 1450 to 1650 nm, as displayed in Figure 1E. The inset presents the electrical field

component |**E**| for the fundamental quasi-transverse (TE) mode at the resonant wavelength.

Given that the strain at the MNP is free under bending, the device core layer is positioned slightly away from the MNP. By doing so, we can maximize the strain exerted on the devices during pure bending while ensuring that it stays within safe parameters and below the failure threshold. This results in a significant strain exerted on the device, leading to a higher level of optical measurands ($\Delta\lambda$) induced by mechanical deformation.[64] The Young's moduli of the thin-film polyimide and SU-8 were experimentally measured to be 2.5 and 2 GPa, respectively. The Young's modulus of silicone varying with strain is obtained through fitting of the Mooney-Rivlin formula and found to be about 0.5 MPa at 1% strain.[71] We employed finite-element modeling (FEM) to simulate the strain distribution between layers under a 1 mm bending radius. Due to the significant difference in Young's modulus between silicone and polyimide or SU-8, each layer has its own MNP, resulting in multiple MNPs in the stack for pure bending, as depicted in Figure 1F. The positive and negative signs of strain represent the device in tension or compression states, respectively. To increase the strain–optical interactions, the core layer of the devices is placed near the surface of SU-8 (top/bottom cladding = 2 μm/18 μm), as indicated by the white solid line in Figure 1F. The MNP is represented by the red dashed line. The setup for strain–optical coupling measurements is exhibited in Figure 1G (Supporting Information Section S1). The optical resonant wavelengths of 1D PhC microcavities are monitored in situ while the flexible chip is bent. It is worth noting that the grating couplers
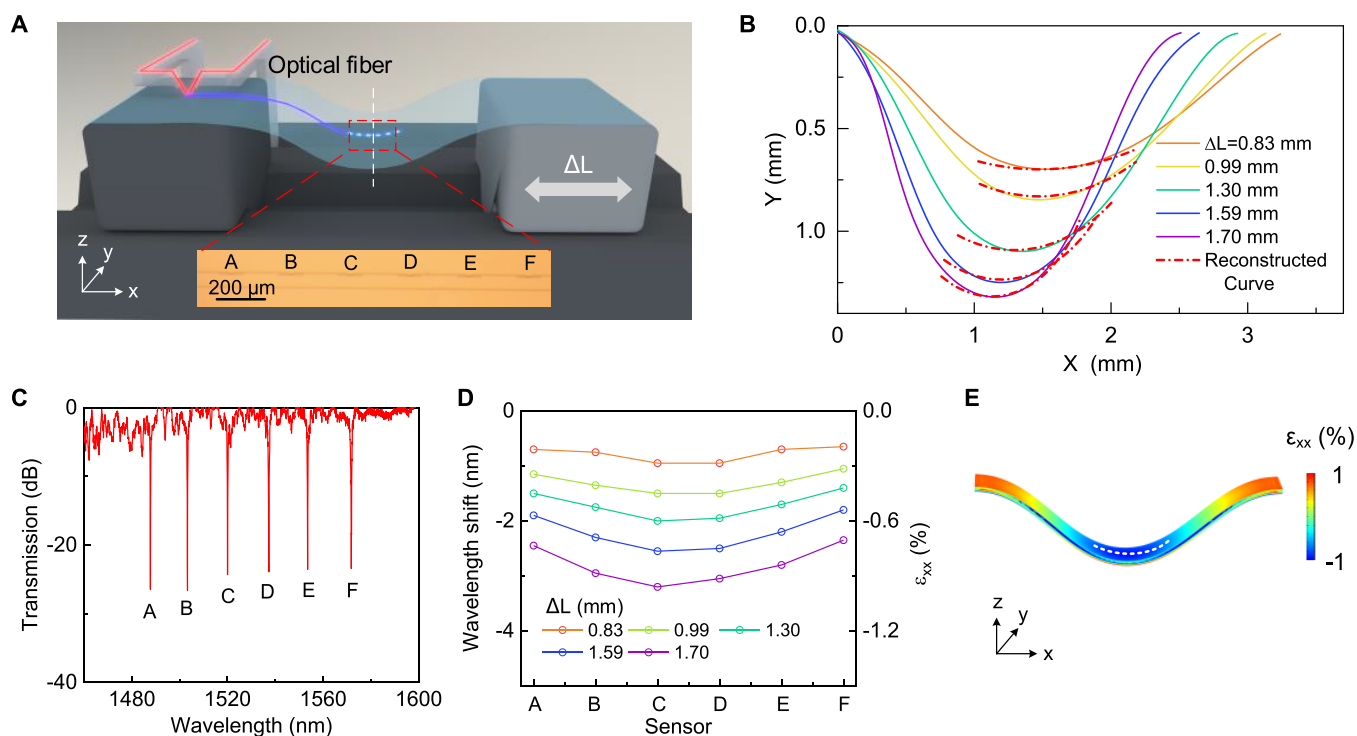
Figure 3. (A) Coupling platform for quasi-distributed strain sensing characterization. Inset shows the microscope image of the sensor array consisting of six cascaded integrated sensors, and the arrow indicates the moving direction of the sample stage. (B) Cross-sectional bending curves of the buckling chip under microscope observation (solid lines) and reconstructed by cascaded sensors (dotted lines) for different moving distances ΔL. (C) Transmission spectrum of the sensor array while the chip is flat without buckling. (D) Resonance dip wavelength shifts and corresponding experienced strains for the six sensors under different bending conditions by changing ΔL. (E) Simulated strain (ε_{xx}) for $\Delta L = 1.7$ mm. The white dashed line indicates the position of the cascaded integrated strain sensors.

are fixed on the static stage, and any coupling efficiency variation induced by the applied strain can be ignored.

The right-angle gauge's transmission spectrum without bending is shown in Figure 2A, where two deep resonant dips corresponding to sensors A and B can be observed in the wavelength range of 1450−1620 nm. The pitches of sensors A and B are 435 and 445 nm, respectively. The 3-dB bandwidth of dip A and dip B is 0.26 and 0.20 nm, while the loaded Q-factors are about 5850 and 7755, respectively. When the distance between the two stages is decreased and the chip is bent along the x-axis with the bending curvature from 0 to 2 mm^{-1} at the lowest point, the resonant dip of sensor A undergoes a blueshift of 3.62 nm, and sensor B shows a redshift of 0.66 nm in its respective resonant wavelength, as depicted in Figure 2B. The wavelength blueshift of sensor A is due to the shrinkage in the lattice constant, as the Bragg grating is positioned along the x-axis, while the wavelength redshift of sensor B is caused by the lattice pitch increment under stretching along the y-axis as per Poisson's theorem. We have observed a nearly perfect linear correlation between the bending curvature of the flexible chip and the wavelength shift, as shown in Figure 2C. Meanwhile, we also calculated the strain by FEM coupled with a rigorous strain−optical coupling theory,[64] revealing the increasing strain along the x-axis ε_{xx} from 0 to −0.92%, as the green line shows in Figure 2C. The strain ε_{xx} under the bending curvatures of 0, 1, and 2 mm^{-1} is illustrated in Figure 2D. Thus, we can obtain the relationship between the resonant wavelength shift of these two sensors and ε_{xx} as shown in Figure 2E. Sensor A possesses the strain sensitivity of 0.39 pm/$\mu\varepsilon$ by the linear fitting with a high R^2 of

0.997, while Sensor B has the strain sensitivity of −0.07 pm/$\mu\varepsilon$ with a high R^2 of 0.996. The letter ε refers to the unit strain.

To evaluate the precision of spectral strain resolution using an optical resonance shift, we define an optical strain-resolving factor as $(\Delta\lambda/\varepsilon)/\delta\lambda$ including the strain sensitivity and spectral resolution,[72] where $\Delta\lambda$ and $\delta\lambda$ are the resonant wavelength shift and 3-dB bandwidth of the resonance, respectively. The strain−optical coupling strategy provides a sensitive measurement of local strain with a detection optical strain-resolving factor of about 2000. Therefore, through the established relationship between the resonant wavelength shift and strain, we can precisely determine the principal strain magnitudes with known directions by such a right-angle gauge to realize biaxial tensile analysis (Supporting Information Section S2). Moreover, the strain gauge is completely EMI-free due to the purely optical effects.

Thanks to the FSR-free spectral response, our proposed 1D PhC microcavity has advanced multiplexing capability. It holds promise as a quasi-distributed sensor by cascading multiple microcavities with different grating pitches, which enables strain and position information encoded into the wavelength-dependent resonant dip, and the resulting wavelength shift can be used to retrieve the quasi-distributed strain information along the cavity section, rendering the integrated sensor a highly flexible and customizable platform for high spatial resolution strain mapping in the range of tens to hundreds of micrometers.

To illustrate the capability of our demonstration, we analyzed the distribution of bending strain in a buckling chip consisting of six cascaded sensors that are arranged in a line with a spacing interval of 110 μm. The sensing units have
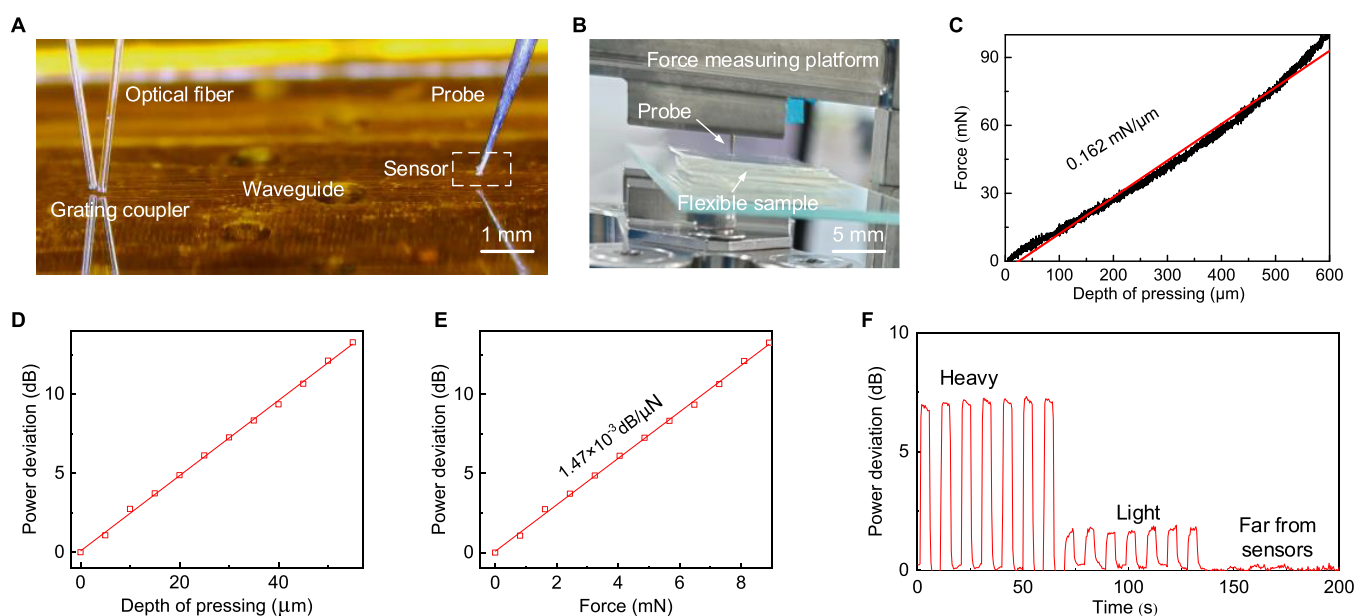
Figure 4. (A) Photograph showing the flexible chip on a plane stage used to characterize the device sensitivity and dynamic performance. The strain was applied via a metal needle probe, and the light was coupled into and out of the waveguide through optical fibers. (B) Photograph of the testing probe loading platform for force calibration. (C) Measured forces at different pressing depths. The red line represents the linear regression model fitted to the original measurement data set. (D) Measured optical power deviation at different pressing depths. (E) Relationship between the received optical power deviation and force applied on the sensor via the metal needle. (F) Dynamic performance of the point force sensor under intermittent heavy and light force loaded by the metal needle and heavy pressure but far from the sensor.

grating pitches ranging from 432 to 452 nm with an increment of 4 nm. As shown in Figure 3A, the chip is loaded on the linear motion stages and the white dashed line indicates the normal line passing the lowest point of the bending curve. Sensors A−C are located to the left of the normal line, while sensors D−F are on the right. The inset shows the microscope image of the strain sensor array. To simulate various cross-sectional bending curves for the buckling sample, the position of the movable stage is adjusted to apply an external lateral force to the chip along the x-axis. As shown in Figure 3B, the solid lines indicate the bending profiles of the buckling chip extracted from the captured images with a lateral microscope.

The curve reconstruction by quasi-distributed strain sensing has been carried out by extracting the wavelength shift of each sensor based on the strain−optical coupling conditions given in Figure 2C. The chip is initially flat (moving distance of the linear motion stage $\Delta L = 0$ mm) to obtain the transmission spectrum of the flexible chip, revealing six resonant dips throughout the entire testing waveband, whose resonant wavelengths have been recorded for calibration (Figure 3C). The temperature stability analysis can be found in Supporting Information Section S3. These dips correspond to six cascaded sensors (A−F) coupled to a single waveguide for the quasi-distributed sensing along the bending curve. The curves reconstructed from the curvature values of the six sensors are depicted by the red dotted line in Figure 3B, which agrees well with the bending profile captured by the camera. The detailed method can be found in Supporting Information Section S4.

In addition, by employing the calibrated strain−optical coupling relation given in Figure 2E, we can obtain the experienced strain (ε_{xx}) for the six sensors at different bending conditions by changing the moving distance ΔL (Figure 3D). For comparison, we calculate the strain distribution of the buckling beam by using FEM based on the extracted cross-sectional bending profile for a moving distance of 1.7 mm, as

shown in Figure 3E, which agrees well with the results of the purple curve in Figure 3D. Therefore, our method enables precise quantification of the quasi-distribution strain in a flexible device undergoing bending with high spatial resolution. By adding more strain sensors, we can achieve a greater number of points and a more comprehensive strain sensing, taking advantage of the abundant spectrum resources with minimal losses.

The high Q-factor of the proposed mechanical sensor contributes to the high sensitivity when using the slope detection method. By tuning the laser to the resonance flank, force-induced resonant wavelength shifts translate to intensity modulations of the output light. Compared to the response wavelength analysis, the slope detection method can obtain higher sensitivity and requires less sampling time, albeit at the cost of a low dynamic range. To demonstrate the capability of resolving small force changes, we measured the collective optical power variation when the chip was placed on a plane stage. Due to the small mode volume of our 1D PhC microcavities, a metal needle probe with about 10-μm tip radius can provide effective external stimuli by touching the surface over the microcavity, as shown in Figure 4A. Coupling loss deviation can be ignored since the sensor is far from the grating coupler and the optical fiber is suspended. Prior to conducting the sensing experiments, it is necessary to determine the forces associated with varying pressing depths. To achieve this, we designed and implemented a platform utilizing the dynamic thermomechanical analyzer (TA-Waters, Massachusetts), as illustrated in Figure 4B, for force calibration. This platform ensures precise static force measurements with a precision of 1 μN and accurate displacement measurements with a precision of 1 nm. The forces applied at different pressing depths were determined experimentally and are represented by the black curve in Figure 4C. By performing linear regression analysis, we have established the relationship

Table 1. Comparison of State-of-the-Art Flexible Force Sensors

working principle	sensing level	unit size	conformal sensing (yes/no)	multiplexed (yes/no)	year
Piezo-resistance	90 μN	5 × 5 mm	Yes	Yes	2021[6]
Piezo-resistance	10 mN	5 × 5 mm	Yes	No	2018[7]
Capacitance	20 mN	4 × 4 mm	Yes	Yes	2018[8]
Magnetoelasticity	0.1 N	0.3 × 0.3 mm	Yes	Yes	2021[9]
Fiber Grating	17.8 mN	20 × 5 mm	No	Yes	2021[32]
Fiber Grating	60 mN	15 × 15 mm	No	Yes	2016[33]
Micro-Nano fiber	1 mN	10 × 10 mm	Yes	No	2021[28]
Micro-Nano fiber	10 μN	0.1 × 0.1 mm	Yes	No	2022[26]
Integrated flexible photonics	13.6 μN	0.11 × 0.03 mm	Yes	Yes	This work

between force and pressing depth with a slope of 0.162 mN/μm.

The collective optical power increases almost linearly with the increasing pressing depth (red line), as shown in Figure 4D. Thus, we attain the force by detecting the optical power deviation with a sensitivity of 1.47×10^{-3} dB/μN, as shown in Figure 4E. Considering the detection accuracy of the photodetector (Santec MPM-215-04-F, ±0.02 dB), we can achieve a detected force level as low as 13.6 μN. The proposed force sensor is a powerful platform for real-time measurement. We characterize the response of the sensor when the probe intermittently touches the surface over or far from the sensor, as shown in Figure 4F. When the probe applies heavy pressure on the sensor, there is a large optical power variation, consistent with an obvious depth change. A small optical power fluctuation can be observed when the probe gently presses the sensor. Although the chip is heavily pressurized, the optical power remains almost unchanged when the probe is far from the sensor. Table 1 shows a comparison of state-of-the-art flexible force sensors. Our sensor demonstrates significant advantages in detecting extremely small force changes with a compact footprint and multiplexing capability for a large-scale sensor matrix, which makes it highly sensitive to slight mechanical deformation with high spatial resolution and massive sensing information.

In summary, we reported an integrated flexible microscale mechanical sensor with FSR-free 1D PhC microcavities. By optimization of the layout of the cascaded cavities, the strain gauge consisting of function units sharing a single bus waveguide can precisely determine principal strain magnitudes with a known direction. The FSR-free feature of the 1D PhC microcavity enables the ease of scalability and flexible configuration to a sensor array or matrix. We investigate the relationship between strain, position information, and wavelength-dependent resonant dips, enabling precise strain quasi-distribution assessment of a buckling beam by using six strain sensors with high spatial resolution. By utilizing the curvature information from six different sensors, we achieve two-dimensional shape sensing of the buckling beam, which is the first successful demonstration of quasi-distribution strain and shape sensing on a waveguide-integrated flexible photonic platform to the best of our best knowledge. The number of strain sensors can be further increased to measure more points, leading to large-scale and high-spatial-resolution sensing. Additionally, the force sensor can also be configured in high-sensitivity mode with real-time measurement, demonstrating a detected force limit as low as 13.6 μN by the slope detection method. The proposed mechanical sensor represents a promising platform for advanced applications such as monitoring cellular behavior in vitro for biomedical research.

■ ASSOCIATED CONTENT

ⓢ Supporting Information

The Supporting Information is available free of charge at https://pubs.acs.org/doi/10.1021/acs.nanolett.3c02239.

Additional results and details for integrated flexible microscale mechanical sensor fabrication and measurement, biaxial strain sensing, temperature stability analysis, and the principle of shape sensing (PDF)

■ AUTHOR INFORMATION

Corresponding Author

Lan Li − *Key Laboratory of 3D Micro/Nano Fabrication and Characterization of Zhejiang Province, School of Engineering, Westlake University, Hangzhou 310030, China; Institute of Advanced Technology, Westlake Institute for Advanced Study, Hangzhou 310024, China;* ⓞ orcid.org/0000-0002-9097-9157; Email: lilan@westlake.edu.cn

Authors

Ye Luo − *Key Laboratory of 3D Micro/Nano Fabrication and Characterization of Zhejiang Province, School of Engineering, Westlake University, Hangzhou 310030, China; Institute of Advanced Technology, Westlake Institute for Advanced Study, Hangzhou 310024, China*

Chunlei Sun − *Key Laboratory of 3D Micro/Nano Fabrication and Characterization of Zhejiang Province, School of Engineering, Westlake University, Hangzhou 310030, China; Institute of Advanced Technology, Westlake Institute for Advanced Study, Hangzhou 310024, China*

Maoliang Wei − *State Key Laboratory of Modern Optical Instrumentation, College of Information Science and Electronic Engineering, Zhejiang University, Hangzhou 310027, China; MOE Frontier Science Center for Brain Science & Brain-Machine Integration, Zhejiang University, Hangzhou 310027, China*

Hui Ma − *State Key Laboratory of Modern Optical Instrumentation, College of Information Science and Electronic Engineering, Zhejiang University, Hangzhou 310027, China; MOE Frontier Science Center for Brain Science & Brain-Machine Integration, Zhejiang University, Hangzhou 310027, China*

Yingchun Wu − *Key Laboratory of 3D Micro/Nano Fabrication and Characterization of Zhejiang Province, School of Engineering, Westlake University, Hangzhou 310030, China; Institute of Advanced Technology, Westlake Institute for Advanced Study, Hangzhou 310024, China*

Zequn Chen − *Key Laboratory of 3D Micro/Nano Fabrication and Characterization of Zhejiang Province, School of Engineering, Westlake University, Hangzhou*

310030, China; Institute of Advanced Technology, Westlake Institute for Advanced Study, Hangzhou 310024, China

Hao Dai − State Key Laboratory of Modern Optical Instrumentation, College of Information Science and Electronic Engineering, Zhejiang University, Hangzhou 310027, China; MOE Frontier Science Center for Brain Science & Brain-Machine Integration, Zhejiang University, Hangzhou 310027, China

Jialing Jian − Institute of Advanced Technology, Westlake Institute for Advanced Study, Hangzhou 310024, China; State Key Laboratory of Modern Optical Instrumentation, College of Information Science and Electronic Engineering, Zhejiang University, Hangzhou 310027, China; orcid.org/0000-0001-6809-6588

Boshu Sun − Institute of Advanced Technology, Westlake Institute for Advanced Study, Hangzhou 310024, China; State Key Laboratory of Modern Optical Instrumentation, College of Information Science and Electronic Engineering, Zhejiang University, Hangzhou 310027, China

Chuyu Zhong − State Key Laboratory of Modern Optical Instrumentation, College of Information Science and Electronic Engineering, Zhejiang University, Hangzhou 310027, China; MOE Frontier Science Center for Brain Science & Brain-Machine Integration, Zhejiang University, Hangzhou 310027, China

Junying Li − State Key Laboratory of Modern Optical Instrumentation, College of Information Science and Electronic Engineering, Zhejiang University, Hangzhou 310027, China; MOE Frontier Science Center for Brain Science & Brain-Machine Integration, Zhejiang University, Hangzhou 310027, China

Kathleen A. Richardson − The College of Optics & Photonics, Department of Materials Science & Engineering, University of Central Florida, Orlando, Florida 32816, United States

Hongtao Lin − State Key Laboratory of Modern Optical Instrumentation, College of Information Science and Electronic Engineering, Zhejiang University, Hangzhou 310027, China; MOE Frontier Science Center for Brain Science & Brain-Machine Integration, Zhejiang University, Hangzhou 310027, China; orcid.org/0000-0001-7432-3644

Complete contact information is available at:
https://pubs.acs.org/10.1021/acs.nanolett.3c02239

Author Contributions

[#]Y.L. and C.S. contributed equally to this work. L.L., H.L., C.S., and Y.L. conceived the project. Y.L., M.W., H.M., Z.C., H.D., and J.J. fabricated these devices. C.S., Y.W., and B.S. designed passive optical devices. Y.L. and Y.W. performed optical measurements. L.L., C.S., K.A.R., C.Z., J.L., and Y.L. analyzed the data and wrote the manuscript. All authors commented on the manuscript.

Notes

The authors declare no competing financial interest.

ACKNOWLEDGMENTS

REFERENCES

(1) Altug, H.; Oh, S. H.; Maier, S. A.; Homola, J. Advances and applications of nanophotonic biosensors. *Nat. Nanotechnol.* **2022**, *17*, 5−16.

(2) Li, J. h.; Chen, J. h.; Xu, F. Sensitive and wearable optical microfiber sensor for human health monitoring. *Adv. Mater. Technol.* **2018**, *3*, 1800296.

(3) Kim, I.; Martins, R. J.; Jang, J.; Badloe, T.; Khadir, S.; Jung, H. Y.; Kim, H.; Kim, J.; Genevet, P.; Rho, J. Nanophotonics for light detection and ranging technology. *Nat. Nanotechnol.* **2021**, *16*, 508−524.

(4) Liang, W.; Ilchenko, V. S.; Savchenkov, A. A.; Dale, E.; Eliyahu, D.; Matsko, A. B.; Maleki, L. Resonant microphotonic gyroscope. *Optica* **2017**, *4*, 114−117.

(5) Bai, H.; Li, S.; Barreiros, J.; Tu, Y.; Pollock, C. R.; Shepherd, R. F. Stretchable distributed fiber-optic sensors. *Science* **2020**, *370*, 848−852.

(6) Chen, S. Y.; Bai, C.; Zhang, C. Y.; Geng, D.; Liu, R. L.; Xie, Y.; Zhou, W. Flexible piezoresistive three-dimensional force sensor based on interlocked structures. *Sensor Actuat. A-Phys.* **2021**, *330*, 112857.

(7) Mu, C. H.; Song, Y. Q.; Huang, W. T.; Ran, A.; Sun, R. J.; Xie, W. H.; Zhang, H. W. Flexible normal-tangential force sensor with opposite resistance responding for highly sensitive artificial skin. *Adv. Funct. Mater.* **2018**, *28*, 1707503.

(8) Zou, Z. N.; Zhu, C. P.; Li, Y.; Lei, X. F.; Zhang, W.; Xiao, J. L. Rehealable, fully recyclable, and malleable electronic skin enabled by dynamic covalent thermoset nanocomposite. *Sci. Adv.* **2018**, *4*, 0508.

(9) Yan, Y. C.; Hu, Z.; Yang, Z. B.; Yuan, W. Z.; Song, C. Y.; Pan, J.; Shen, Y. J. Soft magnetic skin for super-resolution tactile sensing with force self-decoupling. *Sci. Robot.* **2021**, *6*, 8801.

(10) Krause, A. G.; Winger, M.; Blasius, T. D.; Lin, Q.; Painter, O. A high-resolution microchip optomechanical accelerometer. *Nat. Photonics* **2012**, *6*, 768−772.

(11) Zhou, F.; Bao, Y.; Madugani, R.; Long, D. A.; Gorman, J. J.; LeBrun, T. W. Broadband thermomechanically limited sensing with an optomechanical accelerometer. *Optica* **2021**, *8*, 350−356.

(12) Gavartin, E.; Verlot, P.; Kippenberg, T. J. A hybrid on-chip optomechanical transducer for ultrasensitive force measurements. *Nat. Nanotechnol.* **2012**, *7*, 509−514.

(13) Mannsfeld, S. C. B.; Tee, B. C. K.; Stoltenberg, R. M.; Chen, C. V. H. H.; Barman, S.; Muir, B. V. O.; Sokolov, A. N.; Reese, C.; Bao, Z. Highly sensitive flexible pressure sensors with microstructured rubber dielectric layers. *Nat. Mater.* **2010**, *9*, 859.

(14) Yin, B.; Liu, X.; Gao, H.; Fu, T.; Yao, J. Bioinspired and bristled microparticles for ultrasensitive pressure and strain sensors. *Nat. Commun.* **2018**, *9*, 5161.

(15) Westerveld, W. J.; Mahmud, M.; Shnaiderman, R.; Ntziachristos, V.; Rottenberg, X.; Severi, S.; Rochus, V. Sensitive, small, broadband and scalable optomechanical ultrasound sensor in silicon photonics. *Nat. Photonics* **2021**, *15*, 341−345.

(16) Shnaiderman, R.; Wissmeyer, G.; Ülgen, O.; Mustafa, Q.; Chmyrov, A.; Ntziachristos, V. A submicrometre silicon-on-insulator resonator for ultrasound detection. *Nature* **2020**, *585*, 372−378.

(17) Basiri-Esfahani, S.; Armin, A.; Forstner, S.; Bowen, W. P. Precision ultrasound sensing on a chip. *Nat. Commun.* **2019**, *10*, 132.

(18) Missinne, J.; Beneitez, N. T.; Mattelin, M. A.; Lamberti, A.; Luyckx, G.; Van Paepegem, W.; Van Steenberge, G. Bragg-grating-based photonic strain and temperature sensor foils realized using imprinting and operating at very near infrared wavelengths. *Sensors* **2018**, *18*, 2717.

(19) Midolo, L.; Schliesser, A.; Fiore, A. Nano-opto-electro-mechanical systems. *Nat. Nanotechnol.* **2018**, *13*, 11−18.

(20) Liu, T.; Pagliano, F.; van Veldhoven, R.; Pogoretskiy, V.; Jiao, Y.; Fiore, A. Integrated nano-optomechanical displacement sensor with ultrawide optical bandwidth. *Nat. Commun.* **2020**, *11*, 2407.

(21) Zobenica, Z.; van der Heijden, R. W.; Petruzzella, M.; Pagliano, F.; Leijssen, R.; Xia, T.; Midolo, L.; Cotrufo, M.; Cho, Y.; van Otten, F. W. M.; Verhagen, E.; Fiore, A. Integrated nano-opto-electro-mechanical sensor for spectrometry and nanometrology. *Nat. Commun.* **2017**, *8*, 2216.

(22) Guo, J.; Liu, X.; Jiang, N.; Yetisen, A. K.; Yuk, H.; Yang, C.; Khademhosseini, A.; Zhao, X.; Yun, S. H. Highly stretchable, strain sensing hydrogel optical fibers. *Adv. Mater.* **2016**, *28*, 10244−10249.

(23) Coutant, O.; De Mengin, M.; Le Coarer, E. Fabry-Perot optical fiber strainmeter with an embeddable, low-power interrogation system. *Optica* **2015**, *2*, 400−404.

(24) Lyu, C.; Liu, Z.; Huo, Z.; Ge, C.; Cheng, X.; Tam, H. Y. High-sensitivity, high-spatial-resolution distributed strain sensing based on a poly(methyl methacrylate) chirped fiber Bragg grating. *Photonics Res.* **2020**, *8*, 1134−1139.

(25) Zhang, L.; Pan, J.; Zhang, Z.; Wu, H.; Yao, N.; Cai, D.; Xu, Y.; Zhang, J.; Sun, G.; Wang, L.; Geng, W.; Jin, W.; Fang, W.; Di, D.; Tong, L. Ultrasensitive skin-like wearable optical sensors based on glass micro/nanofibers. *Opto-electronic Adv.* **2020**, *3*, 190022.

(26) Yu, W.; Yao, N.; Pan, J.; Fang, W.; Li, X.; Tong, L. M.; Zhang, L. Highly sensitive and fast response strain sensor based on evanescently coupled micro/nanofibers. *Opto-electronic Adv.* **2022**, *5*, 210101.

(27) Yao, N.; Wang, X. Y.; Ma, S. Q.; Song, X. D.; Wang, S.; Shi, Z. X.; Pan, J.; Wang, S. P.; Xiao, J. L.; Liu, H. T.; Yu, L. T.; Tang, Y.; Zhang, Z.; Li, X.; Fang, W.; Zhang, L.; Tong, L. M. Single optical microfiber enabled tactile sensor for simultaneous temperature and pressure measurement. *Photonics Res.* **2022**, *10*, 2040−2046.

(28) Jiang, C. P.; Zhang, Z.; Pan, J.; Wang, Y. C.; Zhang, L.; Tong, L. M. Finger-skin-inspired flexible optical sensor for force sensing and slip detection in robotic grasping. *Adv. Mater. Technol.* **2021**, *6*, 2100285.

(29) Qi, S. S.; Zhang, B.; Zhai, C. C.; Li, Y. C.; Yang, A. P.; Yu, Y.; Tang, D. Y.; Yang, Z. Y.; Luther-Davies, B. High-resolution chalcogenide fiber bundles for longwave infrared imaging. *Opt. Express* **2017**, *25*, 26160−26165.

(30) Wang, Y. M.; Gong, J. M.; Dong, B.; Wang, D. Y.; Shillig, T. J.; Wang, A. B. A large serial time-division multiplexed fiber bragg grating sensor network. *J. Lightwave Technol.* **2012**, *30*, 2751−2756.

(31) Hotate, K.; Enyama, M.; Yamashita, S.; Nasu, Y. A multiplexing technique for fibre bragg grating sensors with the same reflection wavelength by the synthesis of optical coherence function. *Meas. Sci. Technol.* **2004**, *15*, 148−153.

(32) Sun, K.; Li, M.; Wang, S. X.; Zhang, G. K.; Liu, H. B.; Shi, C. Y. Development of a fiber bragg grating-enabled clamping force sensor integrated on a grasper for laparoscopic surgery. *IEEE Sens. J.* **2021**, *21*, 16681−16690.

(33) Guo, Y. X.; Kong, J. Y.; Liu, H. H.; Xiong, H. G.; Li, G. F.; Qin, L. A three-axis force fingertip sensor based on fiber bragg grating. *Sensor Actuat. A-Phys.* **2016**, *249*, 141−148.

(34) Lu, Y. L.; Zhu, T.; Chen, L. A.; Bao, X. Y. Distributed vibration sensor based on coherent detection of phase-OTDR. *J. Lightwave Technol.* **2010**, *28*, 3243−3249.

(35) Peng, F.; Duan, N.; Rao, Y. J.; Li, J. Real-time position and speed monitoring of trains using phase-sensitive OTDR. *IEEE Photonic Technol. L.* **2014**, *26*, 2055−2057.

(36) Qin, J.; Zhang, L.; Xie, W. L.; Cheng, R.; Liu, Z. W. Y.; Wei, W.; Dong, Y. Ultra-long range optical frequency domain reflectometry using a coherence-enhanced highly linear frequency-swept fiber laser source. *Opt. Express* **2019**, *27*, 19359−19368.

(37) Zhou, D. P.; Qin, Z. G.; Li, W. H.; Chen, L.; Bao, X. Y. Distributed vibration sensing with time-resolved optical frequency-domain reflectometry. *Opt. Express* **2012**, *20*, 13138−13145.

(38) Ding, Z. Y.; Du, Y.; Liu, T. G.; Liu, K.; Feng, B. W.; Jiang, J. F. Distributed optical fiber current sensor based on magnetostriction in OFDR. *IEEE Photonic Technol. L.* **2015**, *27*, 2055−2058.

(39) Lee, H.; Hayashi, N.; Mizuno, Y.; Nakamura, K. Slope-assisted brillouin optical correlation-domain reflectometry: proof of concept. *IEEE Photonics J.* **2016**, *8*, 6802807.

(40) Mizuno, Y.; Hayashi, N.; Fukuda, H.; Song, K. Y.; Nakamura, K. Ultrahigh-speed distributed brillouin reflectometry. *Light Sci. Appl.* **2016**, *5*, 16184.

(41) Yao, Y. G.; Kishi, M.; Hotate, K. Brillouin optical correlation domain reflectometry with lock-in detection scheme. *Appl. Phys. Express* **2016**, *9*, 072501.

(42) Lauffenburger, D. A.; Horwitz, A. F. Cell migration: a physically integrated molecular process. *Cell* **1996**, *84*, 359−369.

(43) Sunyer, R.; Conte, V.; Escribano, J.; Elosegui-Artola, A.; Labernadie, A.; Valon, L.; Navajas, D.; García-Aznar, J. M.; Muñoz, J. J.; Roca-Cusachs, P. Collective cell durotaxis emerges from long-range intercellular force transmission. *Science* **2016**, *353*, 1157−1161.

(44) Lee, D. A.; Knight, M. M.; Campbell, J. J.; Bader, D. L. Stem cell mechanobiology. *J. Cell. Biochem.* **2011**, *112*, 1−9.

(45) Tomasek, J. J.; Gabbiani, G.; Hinz, B.; Chaponnier, C.; Brown, R. A. Myofibroblasts and mechano-regulation of connective tissue remodelling. *Nat. Rev. Mol. Cell Biol.* **2002**, *3*, 349−363.

(46) Polacheck, W. J.; Chen, C. S. Measuring cell-generated forces: a guide to the available tools. *Nat. Meth.* **2016**, *13*, 415−423.

(47) Rodrigues, M.; Kosaric, N.; Bonham, C. A.; Gurtner, G. C. Wound healing: a cellular perspective. *Physiol. Rev.* **2019**, *99*, 665−706.

(48) Cheng, G.; Tse, J.; Jain, R. K.; Munn, L. L. Micro-environmental mechanical stress controls tumor spheroid size and morphology by suppressing proliferation and inducing apoptosis in cancer cells. *PLoS One* **2009**, *4*, 4632.

(49) Wang, C. T.; Hsieh, T. H.; Chien, C. C.; Chiang, C. C. Monitoring curing of quasi-isotropic carbon fiber/epoxy composite using fiber bragg grating sensors. *Sensor Mater.* **2016**, *28*, 441−446.

(50) Won, R. In search of new materials. *Nat. Photonics* **2011**, *5*, 139−140.

(51) Floris, I.; Adam, J. M.; Calderon, P. A.; Sales, S. Fiber optic shape sensors: a comprehensive review. *Opt. Lasers Eng.* **2021**, *139*, 106508.

(52) Khan, F.; Denasi, A.; Barrera, D.; Madrigal, J.; Sales, S.; Misra, S. Multi-core optical fibers with bragg gratings as shape sensor for flexible medical instruments. *IEEE Sens. J.* **2019**, *19*, 5878−5884.

(53) Jäckle, S.; Eixmann, T.; Schulz-Hildebrandt, H.; Hüttmann, G.; Pätz, T. Fiber optical shape sensing of flexible instruments for endovascular navigation. *Int. J. Comput. Assist. Radiol. Surg.* **2019**, *14*, 2137−2145.

(54) Shi, C. Y.; Luo, X. B.; Qi, P.; Li, T. L.; Song, S.; Najdovski, Z.; Fukuda, T.; Ren, H. L. Shape sensing techniques for continuum robots in minimally invasive surgery: a survey. *IEEE Trans. Biomed. Eng.* **2017**, *64*, 1665−1678.

(55) Michon, J.; Geiger, S.; Li, L.; Goncalves, C.; Lin, H.; Richardson, K.; Jia, X.; Hu, J. 3D integrated photonics platform with deterministic geometry control. *Photonics Res.* **2020**, *8*, 194−201.

(56) Chen, S.; Zhuo, M. P.; Wang, X. D.; Wei, G. Q.; Liao, L. S. Optical waveguides based on one-dimensional organic crystals. *PhotoniX* **2021**, *2*, 1−24.

(57) Zuo, H.; Yu, S.; Gu, T.; Hu, J. Low loss, flexible single-mode polymer photonics. *Opt. Express* **2019**, *27*, 11152−11159.

(58) Missinne, J.; Kalathimekkad, S.; Van Hoe, B.; Bosman, E.; Vanfleteren, J.; Van Steenberge, G. Stretchable optical waveguides. *Opt. Express* **2014**, *22*, 4168−4179.

(59) Karrock, T.; Gerken, M. Pressure sensor based on flexible photonic crystal membrane. *Biomed. Opt. Express* **2015**, *6*, 4901−4911.

(60) Lu, T.; Wang, C.; Hsiao, C.; Lee, P. Tunable nanoblock lasers and stretching sensors. *Nanoscale* **2016**, *8*, 16769−16775.

(61) Lu, T.-W.; Wu, C.-C.; Lee, P.-T. 1D photonic crystal strain sensors. *ACS Photonics* **2018**, *5*, 2767−2772.

(62) Gan, X.; Clevenson, H.; Englund, D. Polymer photonic crystal nanocavity for precision strain sensing. *ACS Photonics* **2017**, *4*, 1591−1594.

(63) Lu, T.-W.; Wu, C.-C.; Wang, C.; Lee, P.-T. Compressible 1D photonic crystal nanolasers with wide wavelength tuning. *Opt. Lett.* **2017**, *42*, 2267−2270.

(64) Li, L.; Lin, H.; Qiao, S.; Zou, Y.; Danto, S.; Richardson, K.; Musgraves, J. D.; Lu, N.; Hu, J. Integrated flexible chalcogenide glass photonic devices. *Nat. Photonics* **2014**, *8*, 643.

(65) Li, L.; Lin, H.; Qiao, S.; Huang, Y.-Z.; Li, J.-Y.; Michon, J.; Gu, T.; Alosno-Ramos, C.; Vivien, L.; Yadav, A.; Richardson, K.; Lu, N.; Hu, J. Monolithically integrated stretchable photonics. *Light Sci. Appl.* **2018**, *7*, 17138.

(66) Li, L.; Lin, H.; Huang, Y.; Shiue, R.-J.; Yadav, A.; Li, J.; Michon, J.; Englund, D.; Richardson, K.; Gu, T.; Hu, J. High-performance flexible waveguide-integrated photodetectors. *Optica* **2018**, *5*, 44−51.

(67) Chen, F. Y.; Li, X. Y.; Wang, R. H.; Qiao, X. G. Two-dimensional vector accelerometer based on orthogonal bragg gratings inscribed in a standard single-mode fiber cladding. *Opt. Lett.* **2021**, *46*, 2992−2995.

(68) Xu, B.; He, J.; Xu, X.; Liao, C.; Weng, X.; Liu, L.; Qu, J.; Wang, Y. Orthogonal single-mode helical bragg gratings created in fiber cladding for vector bending measurement. *Opt. Lett.* **2023**, *48*, 452−455.

(69) Sun, C.; Zhong, C.; Wei, M.; Ma, H.; Luo, Y.; Chen, Z.; Tang, R.; Jian, J.; Lin, H.; Li, L. Free-spectral-range-free filters with ultrawide tunability across the S+C+L band. *Photonics Res.* **2021**, *9*, 1013−1018.

(70) Sun, C. L.; Yin, Y. X.; Chen, Z. Q.; Ye, Y. T.; Luo, Y.; Ma, H.; Wang, L. C.; Wei, M. L.; Jian, J. L.; Tang, R. J.; Dai, H.; Wu, J. H.; Li, J. Y.; Zhang, D. M.; Lin, H. T.; Li, L. Tunable narrow-band single-channel add-drop integrated optical filter with ultrawide FSR. *Photonix* **2022**, *3*, 12.

(71) Gamonpilas, C.; McCuiston, R. A non-linear viscoelastic material constitutive model for polyurea. *Polymer* **2012**, *53*, 3655−3658.

(72) Choi, J. H.; No, Y. S.; So, J. P.; Lee, J. M.; Kim, K. H.; Hwang, M. S.; Kwon, S. H.; Park, H. G. A high-resolution strain-gauge nanolaser. *Nat. Commun.* **2016**, *7*, 11569.